Self-assembled Pt(II) metallacycles enable precise cancer combination chemotherapy

Pengge Zhang[a], Zhixuan Zhou[b,1], Wen Long[c], Yuping Yan[a], Youshan Li[a], Ting Fu[a,d], Yanlan Liu[a], Zilong Zhao[a,1], Weihong Tan[a,d,e,1], and Peter J. Stang[b,1]

Combination chemotherapy, which involves the simultaneous use of multiple anticancer drugs in adequate combinations to disrupt multiple mechanisms associated with tumor growth, has shown advantages in enhanced therapeutic efficacy and lower systemic toxicity relative to monotherapy. Herein, we employed coordination-driven self-assembly to construct discrete Pt(II) metallacycles as monodisperse, modular platforms for combining camptothecin and combretastatin A4, two chemotherapy agents with a disparate mechanism of action, in precise arrangements for combination chemotherapy. Formulation of the drug-loaded metallacycles with folic acid–functionalized amphiphilic diblock copolymers furnished nanoparticles with good solubility and stability in physiological conditions. Folic acids on the surface of the nanoparticles promote their internalization into cancer cells. The intracellular reductive environment of cancer cells induces the release of the drug molecules at an exact 1:1 ratio, leading to a synergistic anticancer efficacy. In vivo studies on tumor-bearing mice demonstrated the favorable therapeutic outcome and minimal side effects of the combination chemotherapy approach based on a self-assembled metallacycle.

self-assembly | supramolecular coordination complex | combination chemotherapy | targeted cancer therapy | drug delivery

Chemotherapy is a crucial treatment modality of cancer but is often limited by system toxicity and resistance to treatment (1, 2). The coadministration of chemotherapeutic agents targeting multiple mechanisms involved in the initiation and progression of cancers, often termed combination chemotherapy, has emerged as an efficient therapeutic approach due to increasing knowledge of signal pathways and pathological mechanisms associated with cancer proliferation (1, 2). Compared to monochemotherapy, combination chemotherapy has shown promise in overcoming limitations associated with tumor heterogeneity and drug resistance, thus improving therapeutic efficacy (3–5). In addition, combination therapy allows for lower doses of each drug and reduces the adverse effects (3–5). Achieving precise control over the loading of drug molecules remains a significant challenge for combination chemotherapy and is crucial for optimal therapeutic efficacy. Conjugation of two different drug molecules through a covalent linker is a straightforward strategy but is often impeded by difficulties associated with complicated organic synthesis and purification process, as well as limited modularity over the ratio of the drug molecules (6–9). Physical coencapsulation strategies based on nanotechnology, on the other hand, suffer from unsatisfactory coloading efficiency and premature drug leakage during the preparation and transportation processes (7–10). The uncertainty arising from the imprecise loading of drug molecules may lead to a low or unpredictable therapeutic efficacy of the cancer treatment.

Inspired by the elegant self-assembly processes found in nature, coordination-driven self-assembly is an efficient strategy for preparing discrete supramolecular coordination complexes (SCCs). Coordination-driven self-assembly relies on the spontaneous formation of metal–ligand coordination bonds between metal-containing, electron-poor molecular acceptors and electron-rich molecular donors (11). Benefiting from the directional and predictable nature of the coordination bond, the size, shape, and functionalities of SCCs can be precisely modulated. Synergistic interactions between functional moieties incorporated within SCCs can be prepared through rational synthetic design, leading to novel functions that are not obtainable by individual molecular building blocks. SCCs possessing these emerging functions have been leveraged for applications as soft materials (12–15), light-emitting materials (16, 17), catalysts (18, 19), etc. (20–23). Based on the structural and functional tunability of SCCs, we envision that SCCs with a well-defined number and molar ratio of drug molecules can be designed and efficiently prepared, making SCCs an exact and versatile synthetic platform for combination chemotherapy.

Significance

Coadministration of drug molecules in adequate combinations for cancer treatment reduces the doses of each constituent, overcomes resistance mechanisms, and reduces the influence of tumor heterogeneity. Here we utilize coordination-driven self-assembly to prepare platinum(II) metallacycles comprising two drug molecules with distinct anticancer mechanisms in precise ratios. Nanoformulations fabricated by encapsulating the metallacycles into amphiphilic diblock copolymers efficiently enter cancer cells and release the active drug molecules at the exact loading ratio in the reductive cancer microenvironments, leading to a synergistic anticancer effect and therefore a favorable treatment outcome. This study provides a promising supramolecular methodology for the precise organization and delivery of bioactive molecules for inducing synergistic biological effects that maximize therapeutic efficacy.

Herein, we designed and synthesized a suite of platinum(II) metallacycles for precise cancer combination chemotherapy via the coordination-driven self-assembly of molecular precursors decorated with the known chemotherapy drugs camptothecin (CPT) and combretastatin A-4 (CA4). We anticipated the combination of CPT and CA4 would prompt a synergistic effect on their anticancer activity due to their distinct mode of action (24, 25). Self-assembly of CPT-containing molecular donor **1** and CA4-containing molecular acceptor **2** yielded metallacycle **3** comprising both drug molecules in an exact 1:1 molar ratio (Fig. 1A). A reduction-sensitive disulfide bond (26, 27) is introduced as the linker between the drug molecule and the rigid structural backbone of the self-assembled metallacycle. As elevated glutathione concentrations are often observed for cancer cells relative to normal cells (28), the reductive-sensitive linker is anticipated to enhance drug stability in normal physiological conditions and allow for controlled, sustained drug release that reduces systemic toxicity (26, 27). The metallacycle was then encapsulated into amphiphilic diblock copolymers comprising poly(lactic-coglycolic acid) (PLGA) and polyethylene glycol (PEG) to prepare drug-loaded nano-formulation (NF) **3-NF-FA**, which is expected to increase the solubility and stability of the metallacycle (8, 26) and allow for active targeting of tumor cells via the specific interaction between folic acid (FA) and folate receptor (FR) (29). As controls, metallacycles containing only one type of drug or no drug molecule were synthesized and formulated to NFs analogously. Upon internalization into cancer cells via FR-mediated endocytosis, intracellular glutathione triggers the release of active drug molecules from the NFs to enable cytotoxicity (Fig. 1B). In vitro and in vivo studies on the anticancer activity of the NFs demonstrated the advantageous properties of combined chemotherapy by **3-NF-FA**, including high anticancer efficacy and low adverse effects.

Results and Discussion

Self-Assembly of Metallacycles with Precise Drug Loading. The CPT-functionalized dipyridyl molecular donor **1** and CA4-decorated diplatinum molecular acceptor **2** were prepared through simple coupling reactions that connect the carbazole-containing functional precursors to the corresponding drug molecules through a disulfide bond. Both **1** and **2** possess a 90° bite angle between the binding motifs by merit of the rigid, planar carbazole group in their structures. Addition of $AgNO_3$ to the stoichiometric mixture of **1** and **2** in solution, which removes the coordinating I ions on **2** by the formation of AgI, leads to the self-assembly of [2 + 2] metallacycle **3** in almost quantitative yield. As a result, metallacycle **3** features two CPT molecules and two CA4 molecules on its periphery. Using similar approaches, [2 + 2] metallacycles containing two CPT molecules (**4**), two CA4 molecules (**5**), and no drug molecule (**6**) were prepared via the self-assembly between **1**, **2**, or unfunctionalized molecular building blocks (*SI Appendix*, Schemes S1–S8 and Figs. S1–S44)

Multinuclear ^1H and $^{31}P\{^1H\}$ NMR analyses were performed to confirm the formation of metallacycles via coordination. Significant downfield shifts are observed when comparing the pyridyl H_α and H_β from the solutions of **1** and **3** (0.22 ppm for H_α and 0.33 ppm for H_β) (Fig. 2 A and B), suggesting the formation of a Pt-pyridyl N coordination bond that reduced the electron density of the pyridyl protons (30). The broad ^1H signals in **3** are indicative of a large supramolecular ensemble, the tumbling motion of which is slow on the NMR

time scale (30). The $^{31}P\{^1H\}$ NMR spectrum of **3** showed a sharp singlet at 15.81 ppm with concomitant ^{195}Pt satellites (Fig. 2 C and D), indicating the formation of a highly symmetric complex, in which all the P atoms are in an identical chemical environment. Electrospray ionization time-of-flight mass spectrometry (ESI-TOF-MS) studies provide further support for the stoichiometry of the metallacycles. The ESI-TOF-MS spectrum of metallacycle **3** revealed multiple prominent peaks corresponding to the [2 + 2] assembly with charge states resulting from the loss of the ONO_2 counterion. These peaks include $m/z = 1{,}293.8730$, corresponding to $[3 - 4ONO_2]^{4+}$, and $m/z = 1{,}745.4889$, corresponding to $[3 - 3ONO_2]^{3+}$ (Fig. 2E). These peaks were resolved into an isotopic distribution pattern and are in good agreement with their calculated theoretical distributions (Fig. 2 F and G). Similarly, the formation of metallacycles **4** to **6** was confirmed by a combination of NMR and MS analysis (*SI Appendix*). In addition, ultraviolet-visible absorption spectra of the metallacycles were recorded. Characteristic absorption peaks for the CA4 and CPT molecules were detected for the corresponding metallacycles, supporting the successful conjugation of the drug molecules to the metallacycles (*SI Appendix*, Fig. S45). Metallacycle **3** exhibited fluorescence emission originating from the CPT molecule. The fluorescence intensity is significantly lower than that of free CPT molecule under the same conditions (*SI Appendix*, Fig. S46), likely due to the heavy metal effect of the Pt (31).

Preparation of NFs Containing Drug-Loaded Metallacycles. To improve the solubility and stability of the drug-loaded metallacycles in a physiological environment, the FA-decorated diblock copolymer PLGA-*b*-PEG-FA and amphiphilic diblock copolymer PLGA-*b*-PEG were employed in a 1:4 mass ratio to encapsulate the metallacycles. The resulting NFs possessing FA groups on the surface were termed **X-NF-FA**, in which **X** represents the drug-loaded metallacycles. The FA groups were anticipated to facilitate the endocytosis of **X-NF-FA** into cancer cells that frequently have amplified FR expression (29). Based on the molecular structure of the metallacycles, **3-NF-FA** is composed of both CPT and CA4 drug molecules in a 1:1 ratio, **4-NF-FA** and **5-NF-FA** featured only CPT and CA4, respectively, and **6-NF-FA** featured no attached drug molecules. Using the same protocol, NFs with only free CPT (CPT-NF-FA), free CA4 (CA4-NF-FA), and coloaded with CPT and CA4 (CA4/CPT-NF-FA) as small molecules were prepared. In addition, metallacycle-containing NFs without FA (**X-NF**) were prepared by encapsulating the metallacycles with PLGA-*b*-PEG. These NFs were employed as controls in following studies.

The morphological and surface properties of the NFs were then investigated. The zeta potentials of metallacycle **3** and polymer NF (P-NF-FA) prepared by mixing PLGA-*b*-PEG-FA and PLGA-*b*-PEG at a mass ratio of 1:4 were determined to be +20.9 mV and −7.1 mV, respectively (Fig. 3A). In comparison, the zeta potential of **3-NF-FA** was −1.7 mV, suggesting that the metallacycle **3** was successfully encapsulated by the diblock copolymers (Fig. 3A), likely via hydrophobic interactions and electrostatic interactions. The zeta potentials of **3-NF-FA** and P-NF-FA were more positive than those of their counterparts without FA moiety (Fig. 3A and *SI Appendix*, Fig. S47). This phenomenon could be ascribed to the exposure of the pteridine moiety in FA to the buffer (32). Dynamic light scattering (DLS) analysis on **3-NF-FA** revealed an average hydrodynamic diameter of 174.5 nm (Fig. 3B) and was larger than **3-NF** with an average hydrodynamic diameter of 154.6 nm (*SI Appendix*, Fig. S48). Transmission electron microscopy (TEM)
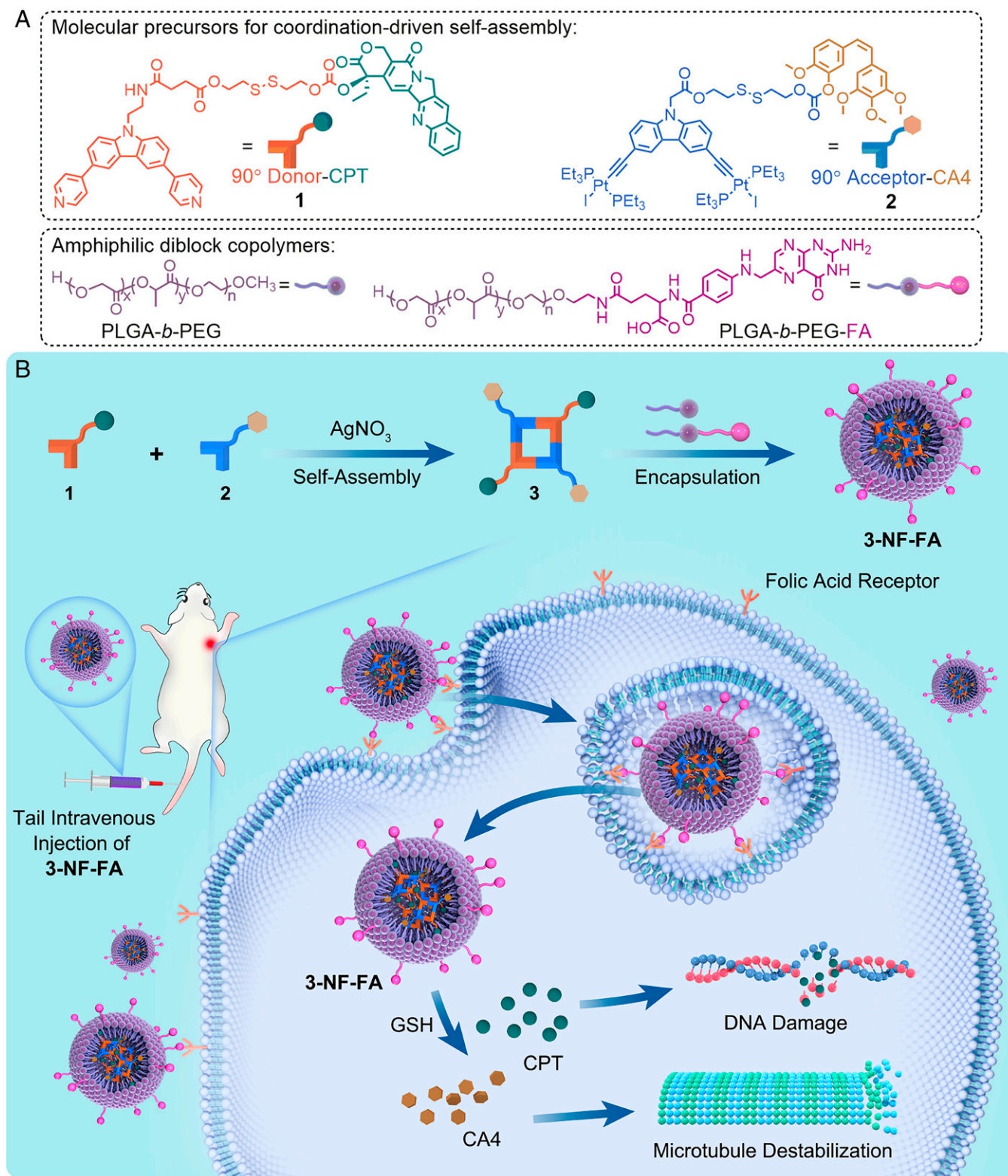
Fig. 1. Preparation of **3-NF-FA** and its anticancer activity via synergistic drug combinations. (*A*) Chemical structures of CPT-containing molecular donor **1**, CA4-containing molecular acceptor **2**, and amphiphilic diblock copolymers PLGA-*b*-PEG and PLGA-*b*-PEG-FA. (*B*) Cartoon illustration of the preparation of **3-NF-FA** and its cellular uptake, intracellular glutathione (GSH)-induced release of active CPT (green), and CA4 (yellow) drug molecules for combined cancer therapy.

analysis on **3-NF-FA** showed spherical nanoparticles with an average diameter of 149 nm (Fig. 3 *C* and *D*). This value is slightly lower than that of DLS studies due to the hydration of the nanoparticles in the DLS experiments. Similar sizes and polydispersity indexes were observed for other NFs comprising metallacycle **4**, **5**, or **6** (*SI Appendix*, Fig. S49 and Table S1).

The metallacycles-containing NFs exhibited good stability in Dulbecco's phosphate-buffered saline (DPBS) or DPBS containing 10% fetal bovine serum over 48 h at 37 °C (*SI Appendix*, Fig. S50), whereas NFs fabricated by encapsulating free drug molecules displayed lower stability and lower loading efficiency (*SI Appendix*, Table S1). This observation is
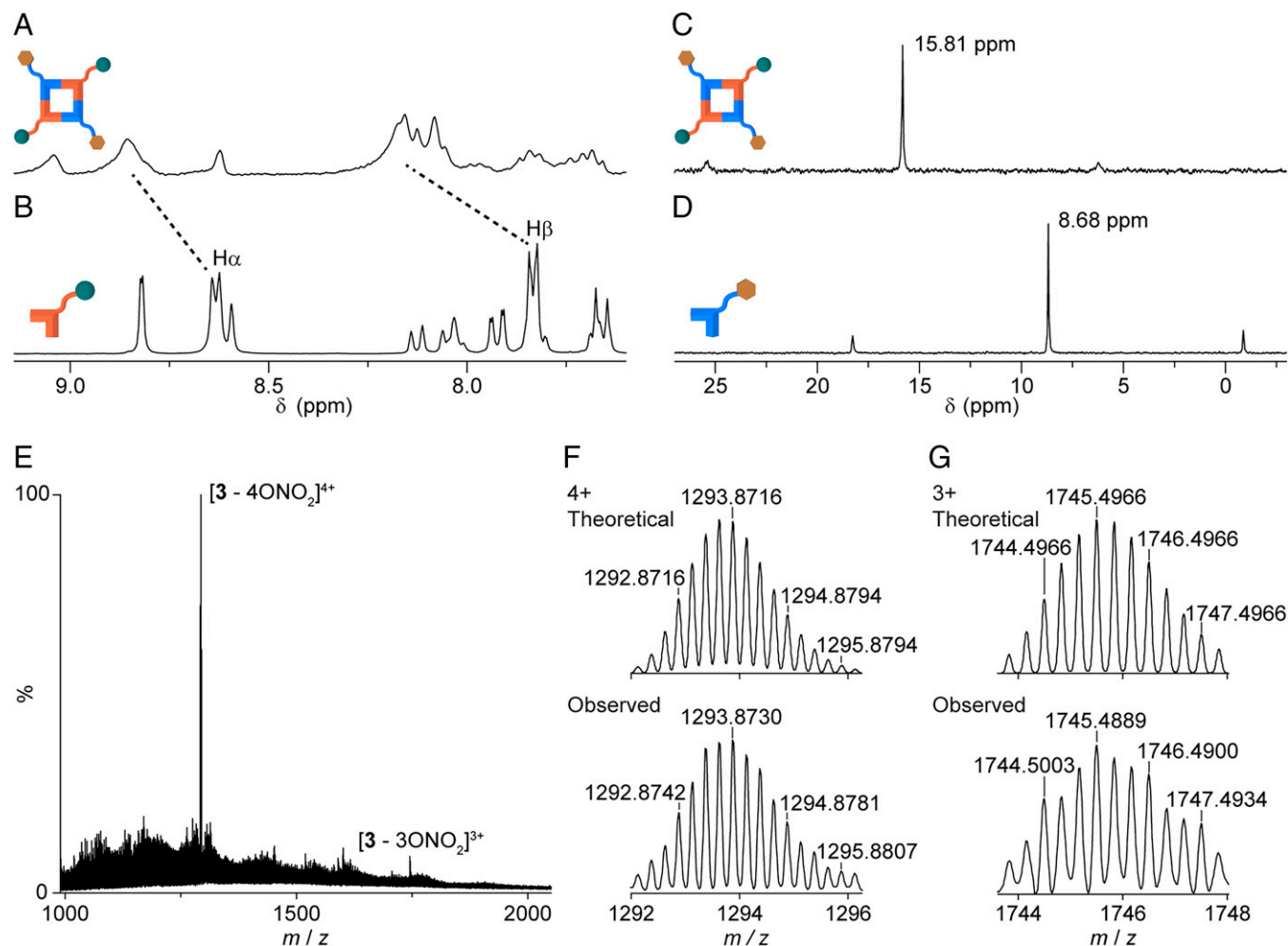
Fig. 2. Characterization of self-assembled metallacycle **3**. (*A* and *B*), Partial ^{1}H NMR spectra (300 MHz, DMSO-d_6, 298 K) of **3** (*A*) and **1** (*B*). (*C* and *D*) Partial ^{31}P{^{1}H} NMR spectra (121 MHz, DMSO-d_6, 298 K) spectra of **3** (*C*) and **2** (*D*). (*E*) ESI-TOF-MS spectrum of **3**. (*F* and *G*) Theoretical (*Top*) and observed (*Bottom*) ESI-TOF-MS spectra of species correspond to [**3** – 4ONO$_2$]$^{4+}$ (*F*) and [**3** – 3ONO$_2$]$^{3+}$ (*G*).

attributed to the formation of bulky, hydrophobic metallacycle by coordination, which promotes the interactions between the metallacycle and the hydrophobic core of the NFs (26, 33).

Precise Release of Anticancer Drugs in Reductive Environments. The cleavage of the disulfide linker in reductive environments and subsequent release of active drug molecules with high precision from the NFs were examined. Glutathione was employed to mimic the reductive tumor microenvironment, where it has been reported that cancer cells possess high intracellular concentrations (0.5 to 10 mM) of glutathione in the cytosol (28). High-performance liquid chromatography (HPLC) analysis showed glutathione efficiently induced the stable and continuous release of active drug molecules from **3-NF-FA** (Fig. 4*A*). In DPBS containing 10 mM glutathione, the release plateaued after 48-h incubation, and more than 80% of the encapsulated drug molecules were found to release in the active form. Conversely, almost no drug release (<5%) was detected after incubation of **3-NF-FA** without glutathione, indicating the drug release of **3-NF-FA** is highly selective toward the reductive tumor microenvironment.

The molar ratio of the drug molecules released by the reductive environment was then determined by comparing the integration of absorption peaks at the retention times corresponding to free drug molecules in the HPLC studies (Fig. 4*B*). The molar ratio between CA4 and CPT released from **3-NF-FA** was in

good agreement with the theoretical ratio of 1:1. In contrast, NF fabricated by coencapsulating free CA4 and CPT molecules (CA4/CPT-NF-FA) could not achieve a 1:1 loading ratio and release ratio based on the HPLC analysis (Fig. 4 *C* and *D*), likely due to the distinct hydrophobic properties between the two molecules. These experiments suggest that the self-assembly formation of drug-containing metallacycle ensures the precise encapsulation and release of drug molecules.

Cellular Uptake, Intracellular Release of Active Drug Molecules, and Cytotoxicity of the NFs. The cellular uptake of the NFs was systematically examined in FR-positive cancer cell lines, including DU145 (*SI Appendix*, Fig. S51), HeLa (34), A549 (35), and HCT116 (36) and FR-negative normal cell line HEK293 (*SI Appendix*, Fig. S51). Inductively coupled plasma MS was employed to obtain quantitative cellular uptake profiles. Prolonged incubation of cells with the NFs resulted in increasing intracellular Pt concentration (Fig. 5 *A* and *B* and *SI Appendix*, Fig. S52), indicating the time-dependent internalization of the NFs. Notably, **3-NF-FA** recorded a higher intracellular Pt concentration than **3-NF** in FR-positive cell lines but not in the FR-negative HEK293 cells. When the FR-positive cells were pretreated with FA, marked decreases were observed in the uptake of **3-NF-FA** (Fig. 5*A* and *SI Appendix*, Fig. S52). In comparison, the pretreatment of HEK293 with free FA exhibited negligible effects on the endocytosis of **3-NF-FA** (Fig. 5*A*). These results
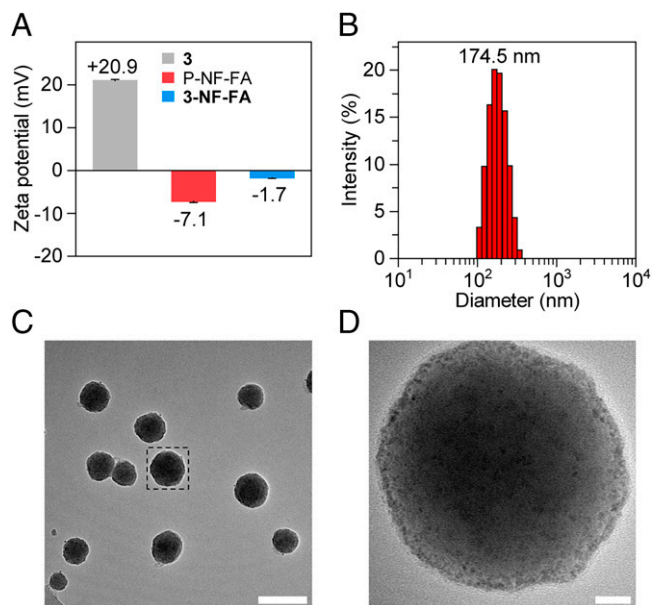
Fig. 3. Characterization of **3-NF-FA**. (*A*) Zeta potentials of **3**, polymer NF formulated by PLGA-*b*-PEG-FA and PLGA-*b*-PEG at a mass ratio of 1:4 (P-NF-FA) and **3-NF-FA**. Data are presented as mean ± SD, *n* = 3. (*B*) DLS analysis on the size distribution of **3-NF-FA**. (*C*) Representative TEM image of **3-NF-FA**. (Scale bar: 200 nm.) (*D*) Magnified TEM image of a nanoparticle circled in *C*. (Scale bar: 20 nm.)

confirmed that the introduction of FA facilitates the cellular uptake of the NFs in cancer cells via FR-mediated endocytosis, resulting in higher drug concentrations in cancer cells.

The intracellular release and distribution of drug molecules were established using confocal laser scanning microscopy

Fig. 4. Precise release of active drug molecules by **3-NF-FA** under the reductive environment. (*A*) Cumulative CPT release by **3-NF-FA** at different concentrations of glutathione (GSH), determined by HPLC. (*B*) HPLC traces of CA4 and CPT from **3-NF-FA** after incubation with 10 mM GSH for 48 h in DPBS (pH = 7.4), an equimolar mixture of CA4 and CPT, CA4, and CPT. (*C*) HPLC traces of an equimolar mixture of CA4 and CPT and NF prepared by coencapsulation of small molecule CA4 and CPT (CA4/CPT-NF-FA). (*D*) Molar ratio of CA4 and CPT released from **3-NF-FA** and CA4/CPT-NF-FA based on their integration of absorption peak in HPLC studies. An equimolar mixture of CA4 and CPT was used as a control (CA4:CPT = 1:1). Data are presented as mean ± SD, *n* = 3.

(CLSM) studies on cancer cells incubated with **3-NF-FA** for varying times. As shown in Fig. 5*C*, intracellular blue fluorescence signals corresponding to free CPT molecules showed a continuous increase in a 6-h incubation period, indicating cellular uptake for the NFs took place in a time-dependent manner. The increase in the fluorescence signal can also be attributed to the intracellular release of CPT molecules from the metallacycle backbone, which significantly reduces the fluorescence quenching effect by the Pt (31). Fluorescence colocalization assay with lysosome-specific LysoTracker dye revealed that CPT molecules were mainly located in the late endosome and lysosome after 2-h incubation. With prolonged incubation, the blue fluorescence signal of CPT in the nucleus gradually increased, suggesting the migration of the released CPT molecules into the nucleus, where CPT inhibits DNA topoisomerase and thus elicits the anticancer activities (24). After 8-h incubation, the fluorescence signal of CPT in the cytoplasm decreased, which might be caused by drug efflux. The release of active CA4 from **3-NF-FA** was examined by fluorescence imaging of tubulin. After 8-h incubation, cancer cells treated with **3-NF-FA** displayed minimal fluorescence signal corresponding to tubulin compared to those treated with DPBS or **4-NF-FA** (Fig. 5*D*), suggesting that tubulin polymerization was inhibited by the microtubule-targeting CA4 (25). These results support the efficient intracellular release of active anticancer drugs from the NFs.

The cytotoxicity of the various NFs was examined using the cell counting kit-8 assay, and the results are summarized in Fig. 5*E* and *SI Appendix*, Fig. S53 and Table S2. For DU145 cells, **3-NF-FA** exhibited the highest cytotoxicity (concentration that inhibits response by 50% [IC_{50}] = 31.67 nM) relative to NFs containing one type of drug molecules (**4-NF-FA** featuring only CPT and **5-NF-FA** featuring only CA4, IC_{50} = 65.11 nM and 148.8 nM, respectively) or metallacycle without drug molecule (**6-NF-FA**, IC_{50} > 3.0 μM) (Fig. 5*E*), indicating a drug synergistic effect on anticancer activity of **3-NF-FA**. The drug combination index (CI) was determined to be 0.70 (*SI Appendix*, Table S3). Apoptosis analysis using annexin-V FITC/propidium iodide dual-staining was employed to provide further insight into the anticancer activity by providing quantitative results for the apoptotic/necrotic status of the cancer cells treated with the NF-FAs. Treatment of **3-NF-FA** evoked the highest level of apoptosis and necrosis (50.14% in total). In comparison, lower populations of apoptotic and necrotic cells were detected when the cells were treated with **3-NF** (34.93%), **4-NF-FA** (29.88%), **5-NF-FA** (9.99%), and **6-NF-FA** (1.23%) (*SI Appendix*, Fig. S54). Cell cycle arrest analysis revealed that **3-NF-FA** inhibits the cell cycle in the G2/M phases (*SI Appendix*, Fig. S55). A similar drug synergistic effect was observed for the anticancer activity of **3-NF-FA** against HCT116 cells (CI = 0.47), whereas an antagonistic effect was detected for HeLa and A549 cell lines (*SI Appendix*, Fig. S53), and lower toxicity was observed against HEK293 cells that lack FRs (Fig. 5*F*). Taken together, these experiments support that self-assembly of **3** and subsequent fabrication of **3-NF-FA** enables the selective delivery and intracellular release of active drug molecules with a precise ratio in cancer cells, which could induce a highly favorable synergistic effect on the anticancer activity.

In Vivo Antitumor Activity of 3-NF-FA. To evaluate the in vivo antitumor activity of **3-NF-FA**, the pharmacokinetics of **3-NF-FA** in normal mice was first determined by analyzing the amount of platinum in blood samples collected at preassigned time points post the intravenous injection of **3-NF-FA** at the tail vein. Cisplatin was used as a control. A longer circulation
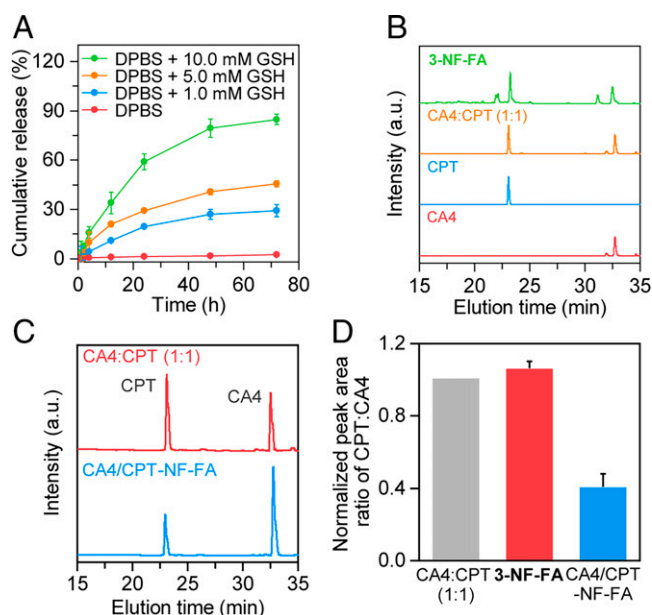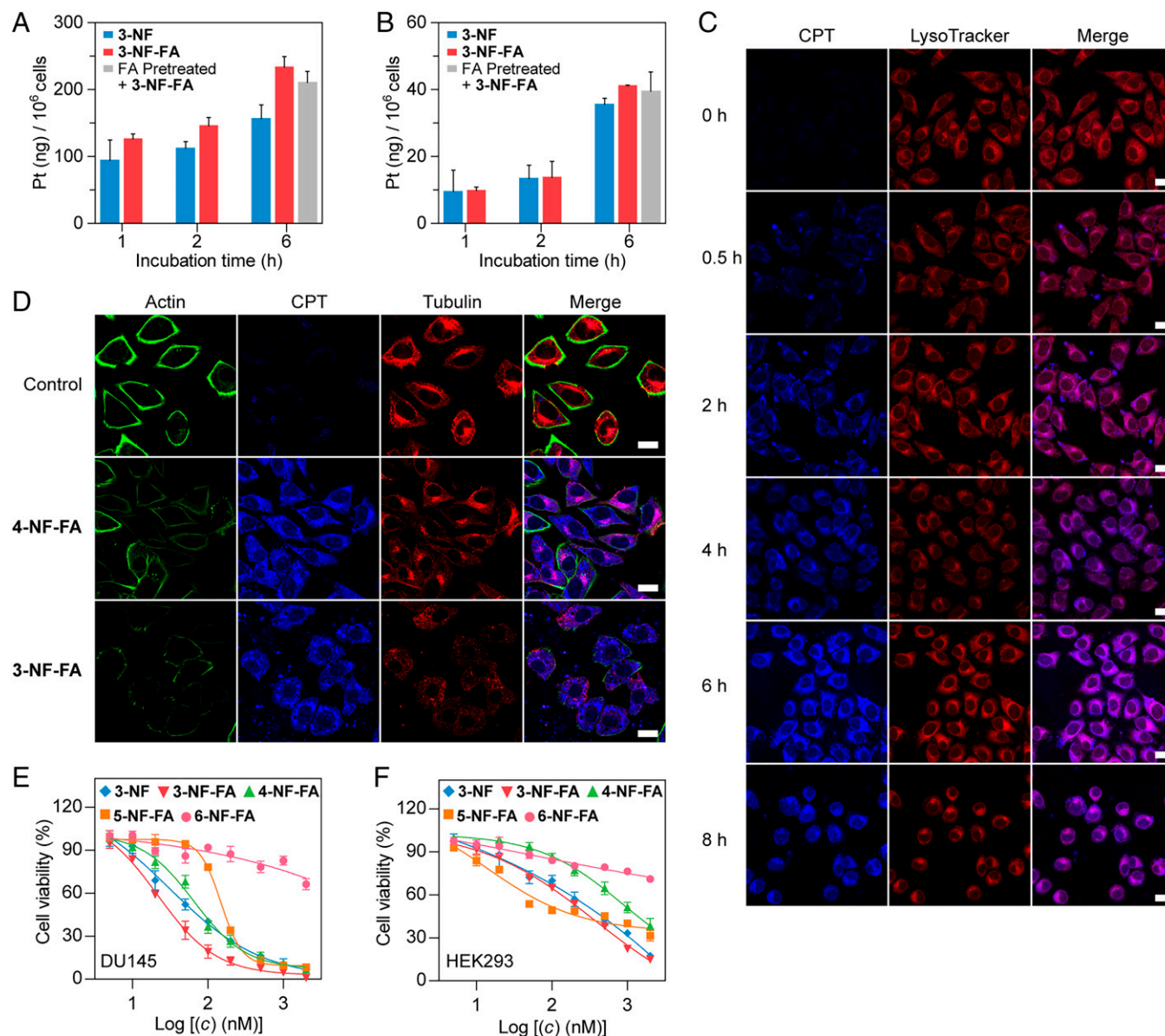
Fig. 5. Cellular uptake, intracellular release of active drug molecules, and cytotoxicity of **3-NF-FA**. (*A* and *B*) Cellular uptake profile of **3-NF-FA** and 3-NF in DU145 cells (*A*) and HEK293 cells (*B*). Data are presented as mean ± SD, *n* = 3. (*C*) CLSM analysis on the intracellular release and distribution of CPT from **3-NF-FA** in DU145 cells in an 8-h incubation. The blue fluorescence and the red fluorescence correspond to CPT and LysoTracker, respectively. (Scale bars: 20 μm.) (*D*) CLSM analysis on the inhibition of tubulin polymerization by CA4 released from **3-NF-FA** in DU145 cells. CPT-loaded **4-NF-FA** and DPBS were used as controls. (Scale bars: 20 μm.) (*E* and *F*) Cytotoxicity of various NFs against DU145 cells (*E*) and HEK293 cells (*F*). Data are presented as mean ± SEM, *n* = 3.

half-life was observed for **3-NF-FA** (6 h) when compared to the small molecule drug cisplatin (2.48 h) (*SI Appendix,* Fig. S56). The prolonged circulation half-life might be ascribed to nanomedicines' enhanced permeability and retention effect and the active targeting by FA, which is highly beneficial for enhancing the therapeutic outcome and reducing side effects of the treatment (37).

The in vivo anticancer performance of the **X-NF-FAs** was then evaluated using DU145 tumor-bearing nude mice. The tumor-bearing mice were classified into five groups (*n* = 4), and each group then received an injection of DPBS, **3-NF-FA** (comprising both CPT and CA4), **4-NF-FA** (featuring only CPT), **5-NF-FA** (featuring only CA4), or **6-NF-FA** (containing metallacycle without drug attachment) at the tail vein once every other day, respectively. After three total injections, the mice were allowed to grow for another 10 d, and the tumor

volume was monitored throughout the experiment (Fig. 6*A* and *SI Appendix,* Fig. S57). The tumors were excised after day 14 and the weights of the tumors were assessed (Fig. 6 *B* and *C*). Mice injected with DPBS displayed rapid growth in tumor volume (1,230 mm³). Among mice treated with the NFs, **3-NF-FA** showed the highest anticancer activity, resulting in a slight increase in tumor volume (207 mm³). In contrast, **4-NF-FA**, **5-NF-FA**, and **6-NF-FA** showed lower anticancer activities (343 mm³, 752 mm³, and 886 mm³ in final tumor volume, respectively). These results support the excellent efficacy of the precise combination chemotherapy by **3-NF-FA**. Slight body-weight increases were observed during the treatment with the NFs (Fig. 6*D*), implying the low system toxicity of the treatment. Further control experiments using NFs loaded with small molecule CPT (CPT-NF-FA), CA4 (CA4-NF-FA), and NF coloaded with two drug molecules (CA4/CPT-NF-FA)
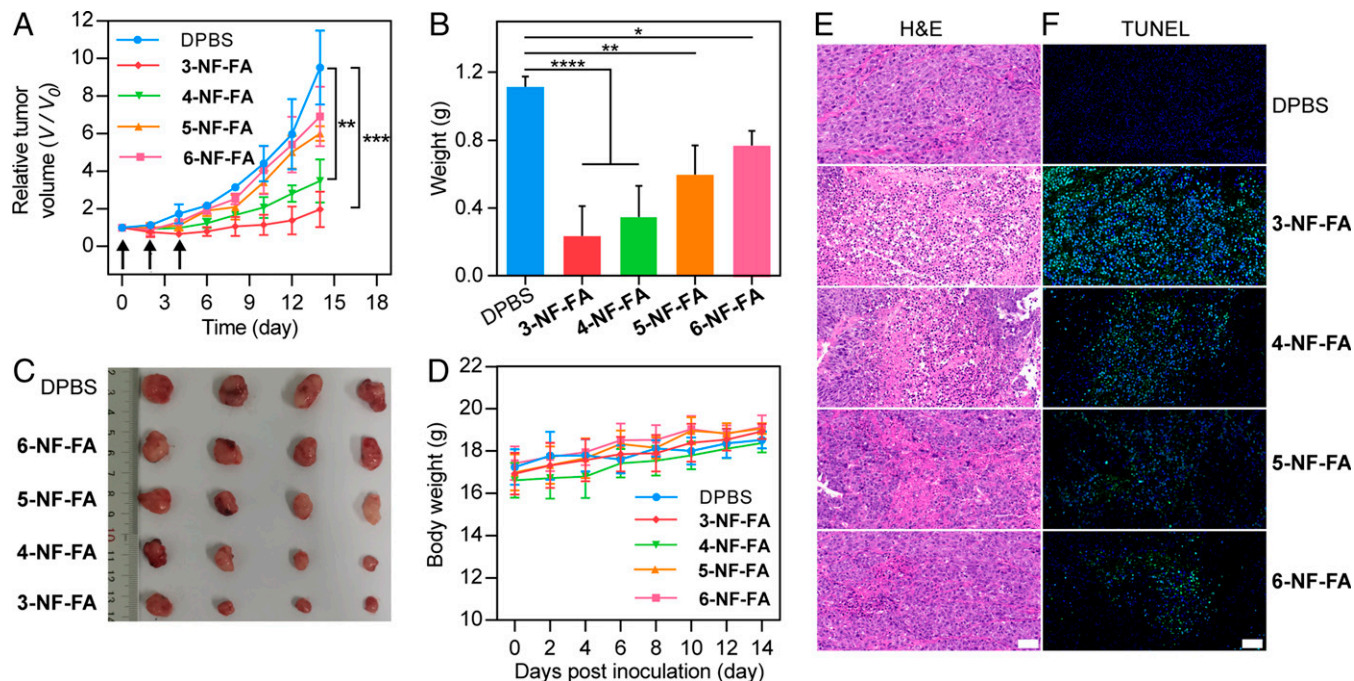
Fig. 6. In vivo antitumor activities of the NFs. (*A*) Relative tumor volume change curves for mice treated with DPBS or various NFs. Arrows indicate the day of injection. (*B*) Tumor weight statistics of mice receiving different treatments. (*C*) Photographs of DU145 tumors harvested from the treated mice on day 14. (*D*) Average body weights of tumor-bearing mice receiving different treatments. (*E*) H&E staining of pathological changes in tumor sections from tumor-bearing mice receiving different treatments. (Scale bar: 50 μm.) (*F*) TUNEL staining assay on cancer cell apoptosis in tumor sections from tumor-bearing mice receiving different treatments. (Scale bar: 50 μm.) All data are presented as mean ± SEM, $n = 4$. Statistical significance was determined by one-way ANOVA with a Tukey post hoc test. $*P < 0.05$, $**P < 0.01$; $***P < 0.001$; $****P < 0.0001$.

confirmed the favorable synergistic anticancer effect by the precise 1:1 loading and release of active drug molecules achieved by **3-NF-FA** (*SI Appendix*, Fig. S58).

The therapeutic efficacy of the NFs was further confirmed by examining the tumor tissue sections from different treatment groups with hematoxylin and eosin histological (H&E) staining assay and terminal deoxynucleotidyl transferase dUTP nick end labeling (TUNEL) staining assay. As shown in Fig. 6 *E* and *F*, **3-NF-FA** effectively induces tumor cell apoptosis during treatment in comparison to other treatments, and no morphological damage was observed in the main organs, including heart, liver, kidney, spleen, and lung (*SI Appendix*, Fig. S59). Furthermore, compared to the blood samples from the tumor-bearing mice treated with DPBS, the level of aspartate aminotransferase, alanine aminotransferase, alkaline phosphatase, creatinine, and urea in the blood samples from the tumor-bearing mice treated with the NFs displayed minimal changes and were in the normal range (*SI Appendix*, Fig. S60), revealing that the NFs elicited no nephrotoxicity and hepatotoxicity during the treatment. Collectively, these results suggest that the precise combination chemotherapy by **3-NF-FA** can efficiently inhibit tumor growth with low systemic adverse effects on healthy tissue in vivo.

Conclusions

In conclusion, we developed self-assembled Pt(II) metallacycles for organizing drug molecules in a defined ratio for combination cancer chemotherapy. The metallacycle ensures a fixed 1:1 molar ratio between the CA4 and CPT drug molecules in the NF process and subsequent intracellular glutathione-induced release. The released drug combination acts synergistically and affords enhanced anticancer activity. In vivo studies demonstrated the enhanced therapeutic effect of the NF relative to monotherapy approaches. Due to the myriad of possible SCCs and the almost limitless modularity and tunability achieved

without significant synthetic penalty (11, 38), the strategy we present herein can be readily expanded for the organization and delivery of bioactive molecules with distinct properties in an exact manner. This feature can be highly beneficial for developing novel combination therapeutic formulations that maximize the therapeutic potentials of bioactive molecules.

Materials and Methods

The details of the materials and methods including synthesis and characterization of the compounds and in vitro and in vivo combined chemotherapy studies on the NFs are described in *SI Appendix*. Animal care and handling procedures were implemented under the guidelines of the Institutional Animal Care and Use Committee of Hunan University and also in accordance with guidelines of the Regional Ethics Committee for Animal Experiments. All animal experiments were approved by the Animal Care and Use Committee of Hunan University (SYXK 2018-0006).

Data Availability. All study data are included in the article and/or *SI Appendix*.

[a]Author affiliations: Molecular Science and Biomedicine Laboratory (MBL), State Key Laboratory of Chemo/Biosensing and Chemometrics, College of Chemistry and Chemical Engineering, Aptamer Engineering Center of Hunan Province, Hunan University, Changsha 410082, China; [b]Department of Chemistry, University of Utah, Salt Lake City, UT 84112; [c]Department of Chemistry and Chemical Engineering, Hunan Normal University, Changsha 410081, China; [d]The Cancer Hospital of the University of Chinese Academy of Sciences (Zhejiang Cancer Hospital), Hangzhou Institute of Medicine (HIM), Chinese Academy of Sciences, Hangzhou 310022, China; and [e]Institute of Molecular Medicine (IMM), Renji Hospital, Shanghai Jiao Tong University School of Medicine and College of Chemistry and Chemical Engineering, Shanghai Jiao Tong University, Shanghai 200240, China

Author contributions: P.Z., Z. Zhou, and Z. Zhao designed research; P.Z., Z. Zhou, and W.L. performed research; P.Z., Z. Zhou, Y.Y., Y. Li, T.F., Y. Liu, Z. Zhao, W.T., and P.J.S. analyzed data; P.Z., Z. Zhou, Z. Zhao, W.T., and P.J.S. wrote the paper; Z. Zhou, Z. Zhao, W.T., and P.J.S. supervised the experiment; and Y. Liu gave advice on preparation of nanoformulations.

1. B. A. Chabner, T. G. Roberts Jr., Timeline: Chemotherapy and the war on cancer. *Nat. Rev. Cancer* **5**, 65–72 (2005).
2. G. Bergers, D. Hanahan, Modes of resistance to anti-angiogenic therapy. *Nat. Rev. Cancer* **8**, 592–603 (2008).
3. S.-Y. Qin, Y.-J. Cheng, Q. Lei, A.-Q. Zhang, X.-Z. Zhang, Combinational strategy for high-performance cancer chemotherapy. *Biomaterials* **171**, 178–197 (2018).
4. J. Jia *et al.*, Mechanisms of drug combinations: Interaction and network perspectives. *Nat. Rev. Drug Discov.* **8**, 111–128 (2009).
5. F. Cheng, I. A. Kovács, A. L. Barabási, Network-based prediction of drug combinations. *Nat. Commun.* **10**, 1197 (2019).
6. L. Zhu *et al.*, Carrier-free delivery of precise drug-chemogene conjugates for synergistic treatment of drug-resistant cancer. *Angew. Chem. Int. Ed. Engl.* **59**, 17944–17950 (2020).
7. H. Chen *et al.*, NIR-light-activated combination therapy with a precise ratio of photosensitizer and prodrug using a host-guest strategy. *Angew. Chem. Int. Ed. Engl.* **58**, 7641–7646 (2019).
8. S. Li *et al.*, Dimeric prodrug-based nanomedicines for cancer therapy. *J. Control. Release* **326**, 510–522 (2020).
9. X. Liang *et al.*, Self-assembly of an amphiphilic janus camptothecin-floxuridine conjugate into liposome-like nanocapsules for more efficacious combination chemotherapy in cancer. *Adv. Mater.* **29**, 1703135 (2017).
10. F. Zhou *et al.*, Molecular engineering-based aptamer-drug conjugates with accurate tunability of drug ratios for drug combination targeted cancer therapy. *Angew. Chem. Int. Ed. Engl.* **58**, 11661–11665 (2019).
11. R. Chakrabarty, P. S. Mukherjee, P. J. Stang, Supramolecular coordination: Self-assembly of finite two- and three-dimensional ensembles. *Chem. Rev.* **111**, 6810–6918 (2011).
12. Y. Gu *et al.*, Photoswitching topology in polymer networks with metal-organic cages as crosslinks. *Nature* **560**, 65–69 (2018).
13. Z. Zhou, X. Yan, T. R. Cook, M. L. Saha, P. J. Stang, Engineering functionalization in a supramolecular polymer: Hierarchical self-organization of triply orthogonal non-covalent interactions on a supramolecular coordination complex platform. *J. Am. Chem. Soc.* **138**, 806–809 (2016).
14. I. Jahović, Y.-Q. Zou, S. Adorinni, J. R. Nitschke, S. Marchesan, Cages meet gels: Smart materials with dual porosity. *Matter* **4**, 2123–2140 (2021).
15. Y. Zhu, W. Zheng, W. Wang, H.-B. Yang, When polymerization meets coordination-driven self-assembly: Metallo-supramolecular polymers based on supramolecular coordination complexes. *Chem. Soc. Rev.* **50**, 7395–7417 (2021).
16. J. Zhao, Z. Zhou, G. Li, P. J. Stang, X. Yan, Light-emitting self-assembled metallacages. *Natl. Sci. Rev.* **8**, nwab045 (2021).
17. X. Tang *et al.*, Endohedral functionalization of chiral metal-organic cages for encapsulating achiral dyes to induce circularly polarized luminescence. *Chem* **7**, 2771–2786 (2021).
18. R. Zaffaroni, N. Orth, I. Ivanović-Burmazović, J. N. H. Reek, Hydrogenase mimics in $M_{12}L_{24}$ nanospheres to control overpotential and activity in proton-reduction catalysis. *Angew. Chem. Int. Ed. Engl.* **59**, 18485–18489 (2020).
19. K. Li *et al.*, Creating dynamic nanospaces in solution by cationic cages as multirole catalytic platform for unconventional C(sp)—H activation beyond enzyme mimics. *Angew. Chem. Int. Ed.* **61**, e202114070 (2021).
20. Z. Zhang *et al.*, Emissive platinum(II) cages with reverse fluorescence resonance energy transfer for multiple sensing. *J. Am. Chem. Soc.* **142**, 2592–2600 (2020).
21. Y. Sun, C. Chen, J. Liu, P. J. Stang, Recent developments in the construction and applications of platinum-based metallacycles and metallacages via coordination. *Chem. Soc. Rev.* **49**, 3889–3919 (2020).
22. D. Zhang, T. K. Ronson, Y.-Q. Zou, J. R. Nitschke, Metal–organic cages for molecular separations. *Nat. Rev. Chem.* **5**, 168–182 (2021).
23. H. Sepehrpour, W. Fu, Y. Sun, P. J. Stang, Biomedically relevant self-assembled metallacycles and metallacages. *J. Am. Chem. Soc.* **141**, 14005–14020 (2019).
24. C. J. Thomas, N. J. Rahier, S. M. Hecht, Camptothecin: Current perspectives. *Bioorg. Med. Chem.* **12**, 1585–1604 (2004).
25. G. G. Dark *et al.*, Combretastatin A-4, an agent that displays potent and selective toxicity toward tumor vasculature. *Cancer Res.* **57**, 1829–1834 (1997).
26. L. Su *et al.*, Chemical design of both a glutathione-sensitive dimeric drug guest and a glucose-derived nanocarrier host to achieve enhanced osteosarcoma lung metastatic anticancer selectivity. *J. Am. Chem. Soc.* **140**, 1438–1446 (2018).
27. J. D. Bargh, A. Isidro-Llobet, J. S. Parker, D. R. Spring, Cleavable linkers in antibody-drug conjugates. *Chem. Soc. Rev.* **48**, 4361–4374 (2019).
28. R. Mo, Z. Gu, Tumor microenvironment and intracellular signal-activated nanomaterials for anticancer drug delivery. *Mater. Today* **19**, 274–283 (2016).
29. J. Sudimack, R. J. Lee, Targeted drug delivery via the folate receptor. *Adv. Drug Deliv. Rev.* **41**, 147–162 (2000).
30. Q.-F. Sun *et al.*, Self-assembled M24L48 polyhedra and their sharp structural switch upon subtle ligand variation. *Science* **328**, 1144–1147 (2010).
31. M. L. Saha, X. Yan, P. J. Stang, Photophysical Properties of organoplatinum(II) compounds and derived self-assembled metallacycles and metallacages: Fluorescence and its applications. *Acc. Chem. Res.* **49**, 2527–2539 (2016).
32. Z. Szakács, B. Noszál, Determination of dissociation constants of folic acid, methotrexate, and other photolabile pteridines by pressure-assisted capillary electrophoresis. *Electrophoresis* **27**, 3399–3409 (2006).
33. X. Guo *et al.*, Dimeric drug polymeric micelles with acid-active tumor targeting and FRET-traceable drug release. *Adv. Mater.* **30**, 1705436 (2018).
34. Y. Peng *et al.*, Smart human-serum-albumin-As₂O₃ nanodrug with self-amplified folate receptor-targeting ability for chronic myeloid leukemia treatment. *Angew. Chem. Int. Ed. Engl.* **56**, 10845–10849 (2017).
35. S. Santra, C. Kaittanis, O. J. Santiesteban, J. M. Perez, Cell-specific, activatable, and theranostic prodrug for dual-targeted cancer imaging and therapy. *J. Am. Chem. Soc.* **133**, 16680–16688 (2011).
36. Z. C. Soe *et al.*, Folate-targeted nanostructured chitosan/chondroitin sulfate complex carriers for enhanced delivery of bortezomib to colorectal cancer cells. *Asian J Pharm Sci* **14**, 40–51 (2019).
37. J. Shi, P. W. Kantoff, R. Wooster, O. C. Farokhzad, Cancer nanomedicine: Progress, challenges and opportunities. *Nat. Rev. Cancer* **17**, 20–37 (2017).
38. T. R. Cook, V. Vajpayee, M. H. Lee, P. J. Stang, K. W. Chi, Biomedical and biochemical applications of self-assembled metallacycles and metallacages. *Acc. Chem. Res.* **46**, 2464–2474 (2013).